Research Article

Nano Research
2022, 15(10): 8846–8856

ISSN 1998-0124 CN 11-5974/O4
https://doi.org/10.1007/s12274-022-4614-x

Reduction-induced interface reconstruction to fabricate $MoNi_4$-based hollow nanorods for hydrazine oxidation assisted energy-saving hydrogen production in seawater

Lili Guo[1], Qingping Yu[1], Xuejun Zhai[1,3], Jingqi Chi[1,2] (✉), Tong Cui[1], Yu Zhang[1], Jianping Lai[1], and Lei Wang[1,3] (✉)

[1] *Key Laboratory of Eco-chemical Engineering, Key Laboratory of Optic-electric Sensing and Analytical Chemistry of Life Science, Taishan Scholar Advantage and Characteristic Discipline Team of Eco Chemical Process and Technology, College of Chemistry and Molecular Engineering, Qingdao University of Science and Technology, Qingdao 266042, China*
[2] *College of Chemical Engineering, Qingdao University of Science and Technology, Qingdao 266042, China*
[3] *College of Environment and Safety Engineering, Qingdao University of Science and Technology, Qingdao 266042, China*

Received: 26 February 2022 / **Revised:** 30 May 2022 / **Accepted:** 31 May 2022

ABSTRACT

Seawater electrolysis could address the water scarcity issue and realize the grid-scale production of carbon-neutral hydrogen, while facing the challenge of high energy consumption and chloride corrosion. Thermodynamically more favorable hydrazine oxidation reaction (HzOR) assisted water electrolysis is efficiency for energy-saving and chlorine-free hydrogen production. Herein, the MoNi alloys supported on MoO_2 nanorods with enlarged hollow diameter on Ni foam (MoNi@NF) are synthesized, which is constructed by limiting the outward diffusion of Ni via annealing and thermal reduction of $NiMoO_4$ nanorods. When coupling HzOR and hydrogen evolution reaction (HER) by employing MoNi@NF as both anode and cathode in two-electrode seawater system, a low cell voltage of 0.54 V is required to achieve 1,000 mA·cm^{-2} and with long-term durability for 100 h to keep above 100 mA·cm^{-2} and nearly 100% Faradaic efficiency. It can save 2.94 W·h to generate per liter H_2 relative to alkaline seawater electrolysis with 37% lower energy equivalent input.

KEYWORDS

MoNi@NF hollow nanorods, seawater splitting, hydrazine oxidation reaction, energy-saving hydrogen production

1 Introduction

The current rapidly increasing global energy consumption and worsening environmental problems stimulate an increasing demand for clean and sustainable hydrogen energy [1–3]. Hydrogen production by electrocatalytic water splitting is a promising strategy to provide green fuel energy in terms of renewables compatibility, processing efficiency, and carbon neutrality [4]. Seawater as infinite resource accounts for ~ 96.5% of the total water supply, providing unlimited hydrogen without relying on the scarce freshwater resource, and electrocatalytic seawater can achieve "hits two birds with one stone" since it can realize hydrogen generation and seawater desalination simultaneously [5, 6], so seawater splitting is ideal for low-cost and large-scale hydrogen production [7–9]. Similar to purified water splitting, seawater splitting involves two half-reactions that the hydrogen evolution reaction (HER) occurs at the cathode and the oxygen evolution reaction (OER) occurs at the anode [10]; differently, the key challenge of competitive chlorine evolution reaction (ClER) may occur on the anode, and the formed corrosive hypochlorite can induce anode corrosion and environmental pollution to reduce the electrolysis sustainability and efficiency [11–13]. According to the theoretical calculation, the voltage required to generate hypochlorite in seawater ($Cl^- + 2OH^- = ClO^- + H_2O + 2e^-$) under alkaline conditions is about 480 mV higher than that of anodic OER [14]. Therefore, the kinetic overpotential of electrocatalyst can only reach a value of 480 mV without producing hypochlorite in the OER process, which is not up to industrial level with the large current density even exceeding 1,000 mA·cm^{-2} [15]. Due to the four-electron-transfer reaction ($4OH^- \rightarrow 2H_2O + O_2 + 4e^-$, 1.23 V vs. reversible hydrogen electrode (RHE)) of OER [16, 17], the overall seawater splitting efficiency is largely restricted, which results in the high oxidation potential and sluggish kinetics [18, 19]. Therefore, there is an urgent demand to develop alternative strategies to decrease electricity demand and achieve energy-saving hydrogen production in seawater [20]. According to previous reports, the anodic OER can be replaced by the thermodynamically more advantageous small molecule oxidation [21–23]. The hydrazine oxidation reaction (HzOR, $N_2H_4 + 4OH^- \rightarrow N_2 + 4H_2O + 4e^-$, −0.33 V vs. RHE) is a representative reaction for the oxidation of small molecules, and its theoretical potential is only −0.33 V vs. RHE, which is much lower than that of OER (1.23 V vs. RHE) and ClER (1.71 V vs. RHE) in seawater [24, 25]. Therefore, the use of electrocatalysis HzOR is a promising method for energy-saving hydrogen production, and it can simultaneously realize the rapid removal of hydrazine from industrial wastewater without the use

Address correspondence to Jingqi Chi, chijingqi@qust.edu.cn; Lei Wang, inorchemwl@126.com

of additional oxidants (such as Fenton's reagent) or complex separation technique [26]. Additionally, coupling HER with HzOR realizes the generation of N_2 as the only by-product, which offers a potential and green method for removing hydrazine from present industrial sewage [27, 28]. Although there have been advances in combing HzOR and HER in purified water, there are few studies on coupling HzOR with HER in seawater electrolysis. Therefore, it is of great significance to explore the dual-function electrocatalyst that integrates HzOR and HER into the seawater electrolysis system [26]. Employing HzOR into seawater electrolysis system can not only realize energy-saving hydrogen production but also promote the removal of hydrazine from industrial wastewater, bringing the huge benefits of environmental sustainability.

Traditional electrochemical water electrolysis of two semi-reactions relies primarily on the use of precious metal-based electrocatalysts (e.g., Pt for HER, IrO_2 and RuO_2 for OER) to reduce the overpotentials and achieve a relatively high energy conversion efficiency [29, 30]. However, these disadvantages of noble-metals, such as high cost, the mismatch of optimum pH of electrolyte, scarcity, and poor stability, greatly limit their widespread applications [8, 31, 32]. So it is urgent to develop highly efficient and durable alternatives with low cost and the bifunctional capability for catalyzing both the HER and HzOR in seawater. Recently, various Ni or Mo-based compounds have been reported as active electrocatalysts for water electrolysis. Among the MoNi-based compounds, Ni atoms serve as excellent water dissociation sites, and Mo atoms possess superior hydrogen adsorption properties [33]. On the other hand, MoNi alloy has been reported to induce hydrogen spillover in heterogeneous catalysts, so it has been regarded as potential catalyst to boost HER performance for heterogeneous catalysts. Moreover, oxygen spillover can be observed in MoO_x species, so MoO_x species can accelerate oxygen spillover to accelerate the transformation of oxygen intermediate to O_2 [34–36]. Therefore, MoNi alloys coupled with MoO_x species are considered as efficient catalysts to reduce the energy barrier of the overall water electrolysis and accelerate the sluggish reaction kinetics in alkaline solutions [37, 38]. However, synthesizing the MoNi alloys and MoO_x hybrids with unique structures to expose more active species and with high activity and stability for HER and HzOR in seawater is still significant and challenging.

Herein, the MoNi alloys supported on Mo oxides hollow nanorods grown on NF (MoNi@NF) as highly efficient bifunctional electrocatalyst have been successfully synthesized via a facile annealing followed by thermal reduction of as-prepared $NiMoO_4$ nanorods. The as-prepared MoNi@NF with enlarged hollow structure integrate the merits of highly active MoNi alloys, interface engineering, and well-dispersed hollow nanorods, which endow the remarkable bifunctional electrocatalytic activities and stability toward both HER and HzOR in alkaline water and seawater system. The hollow nanorods catalyst achieves not only ultralow working potential of only 240 and 470 mV at 1,000 $mA{\cdot}cm^{-2}$ for HER and HzOR, respectively, but also active overall hydrazine splitting (OHzS) performance in seawater electrolysis by coupling HzOR and HER in a two-electrode seawater system, with a voltage of mere 0.54 V at 1,000 $mA{\cdot}cm^{-2}$, which is 1.51 V lower than that in hydrazine-free system, and with remarkable long-term stability for at least 100 h to keep above 100 $mA{\cdot}cm^{-2}$. Moreover, the MoNi@NF-based electrodes for HzOR in seawater can save 2.94 W·h to generate per liter H_2 relative to alkaline seawater electrolysis with 37% lower energy equivalent input. Our work presents an economic approach toward the synthesis of MoNi alloys-based electrocatalysts for carbon neutral and stable energy-saving hydrogen production via seawater splitting.

2 Experimental section

2.1 Chemical and materials

Nickel nitrate hexahydrate ($Ni(NO_3)_2{\cdot}6H_2O$) and sodium molybdate dehydrate ($Na_2MoO_4{\cdot}2H_2O$) were purchased from Aladdin Industrial Corporation. All of the chemicals were used directly without further purification. Ultrapure Milli-Q water was utilized to prepare electrolytes and wash samples

2.2 Materials synthesis

2.2.1 *Synthesis of NiMoO-precursor*

First, three pieces (1 cm × 2 cm) of nickel foam (NF) were cleaned using 0.1 M H_2SO_4, acetone solution, and ethanol solution in an ultrasonic bath for 20 min, respectively, to remove the oxide layer and impurities that may exist on the surface. Then, the cleaned NFs were dried in a vacuum oven for 20 min. Then, 1 mmol $Ni(NO_3)_2{\cdot}6H_2O$ and 1 mmol $Na_2MoO_4{\cdot}2H_2O$ were dissolved in 30 mL deionized water under stirring for 40 min to obtain the uniform solution. Then, the three dried NFs were subsequently immersed into 50 mL Teflon-lined stainless autoclave and heated at 160 °C for 6 h. After cooling to room temperature, the as-obtained NiMoO-precursor grown on nickel foam was taken out and washed with ethanol and de-ionized (DI) water for several times.

2.2.2 *Synthesis of $NiMoO_4$@Ni*

$NiMoO_4$@Ni was prepared by annealing the as-synthesized NiMoO-precursor in N_2 atmosphere at 450 °C for 3 h with a heating rate of 1 $°C{\cdot}min^{-1}$.

2.2.3 *Synthesis of MoNi@NF*

MoNi@NF was prepared by thermal reduction of the as-synthesized $NiMoO_4$@Ni in H_2/Ar atmosphere at 500 °C for 2 h with a heating rate of 2 $°C{\cdot}min^{-1}$. The mass loading of MoNi@NF was determined to be 1.0 $mg{\cdot}cm^{-2}$.

2.2.4 *Synthesis of MoNi + H_2/Ar@NF control samples*

MoNi + H_2/Ar@NF as control samples were prepared by directly thermal reduction of the as-synthesized NiMoO-precursor in H_2/Ar atmosphere at 500 °C for 2 h with a heating rate of 2 $°C{\cdot}min^{-1}$.

2.3 Materials characterization

Scanning electron microcopy (SEM) was utilized to characterize the structure of the catalysts and its accelerating voltage was set at 10 kV. Transmission electron microcopy (TEM) and TEM elemental mappings were used to characterize the morphologies of the catalysts and spatial distribution of elements on a JEM-F200 with the accelerating voltage of 200 kV. X-ray diffraction (XRD) analysis was recorded on the X'Pert PRO MPD at a scanning rate of $1°{\cdot}min^{-1}$ in the 2θ range from 5° to 90°. X-ray photoelectron spectroscopy (XPS) measurements were operated to insure the superficial chemical states by the AXIS SUPRA with a monochromatic Al Kα source at 15 mA and 14 kV. The spectrum was calibrated by carbon 1s spectrum, and its main line was set to 284.6 eV. *In situ* potential-dependent Raman spectroscopy towards HER and HzOR was programmed under applied potentials in 1.0 M KOH + seawater + 0.5 M N_2H_4. Raman spectroscopy was conducted on a Renishaw inVia Raman microscope with the excitation laser of 532 nm.

2.4 Electrochemical measurements

Electrochemical tests were carried out by a Gamry Reference 3000

with a three-electrode system. Saturated calomel electrode (SCE, saturated KCl aqueous solution) was used as reference electrode, while the graphite rod and platinum electrodes were used as counter electrodes for HER and OER, respectively. The as-prepared samples with the size of 1 cm × 1 cm were directly used as working electrodes. To prepare Pt/C and RuO_2 electrodes, 5 mg Pt/C was uniformly dispersed in a solution containing 500 μL of DI water, 495 μL of ethanol, and 5 μL of Nafion mixed solution by sonication for 30 min to form an ink. After dipping, the homogeneous ink mixture was dropped onto a clean NF (1.0 cm × 2.0 cm) and dried in an oven. RuO_2 electrodes were obtained using the same method. All potentials in the text were based on the RHE $E_{RHE} = E_{SCE} + 0.059pH + 0.243$. The electrochemical activities of all prepared electrodes were firstly characterized by linear sweep voltammetry (LSV) for HER, OER, and HzOR at a scan rate of 5 $mV·s^{-1}$ with *iR* compensation in 1.0 M KOH, 1.0 M KOH + 0.5 M NaCl, 1.0 M KOH + seawater, or 1.0 M KOH + seawater + 0.5 M N_2H_4. The seawater used in the experiment was taken from the Shilaoba Beach in Qingdao, China, and was filtered in the laboratory with a water-based filtration membrane with a pore size of 0.2 μm. The main components of the seawater were Na^+, K^+, Ca^{2+}, Mg^{2+} cations, and Cl^- anions. Due to the fact that we explored the performance of seawater splitting in the alkaline seawater system, Ca^{2+} and Mg^{2+} cations would be converted into precipitates after adding KOH. We took the supernatant for further experiments. Electrochemical impedance spectroscopy (EIS) measurements were carried out in a frequency range from 0. 1 Hz to 100 kHz by applying an alternating current (AC) voltage with an amplitude of 5 mV. Chronoamperometric *i*–*t* tests were recorded to test the stability of MoNi@NF in different solutions. The Faradic efficiency (FE) is the ratio of the amount of experimentally evolved hydrogen to that of the theoretically expected hydrogen by the water drainage method. The relevant equations are provided as below $FE = N_{ex}/N_{th}$, $N_{ex} = V/V_m$, and $N_{th} = Q/(n \times F)$, where N_{ex} is the mole number of hydrogen or oxygen actually generated; N_{th} is the theoretical mole number of hydrogen or oxygen; V is the actual volume of gas collected; V_m is 22.4 $L·mol^{-1}$ under standard conditions; Q is the total charge; n is 2 for HER (4 for OER); F is the Faradaic constant (96,485.3 $C·mol^{-1}$).

3 Results and discussion

3.1 Synthesis and characterization of MoNi@NF hollow nanorods

Figure 1(a) presents the synthesis procedure of the hollow MoNi@NF nanorods, where commercial NF with smooth surface is used as conductive and three-dimensional support (Figure S1 in the Electronic Supplementary Material (ESM)). The hollow MoNi@NF nanorods are synthesized through a hydrothermal-annealing-reduction process, and Figs. 1(b)–1(g) display the typical morphology and structure of these various catalysts. First, the $NiMoO_4$ precursor with dense nanorods-like morphology vertically aligned on the NF (NiMoO-precursor) is obtained by the hydrothermal reaction of $Na_2MoO_4·2H_2O$ and $Ni(NO_3)_2·6H_2O$, leading to one-dimensional solid nanorods with

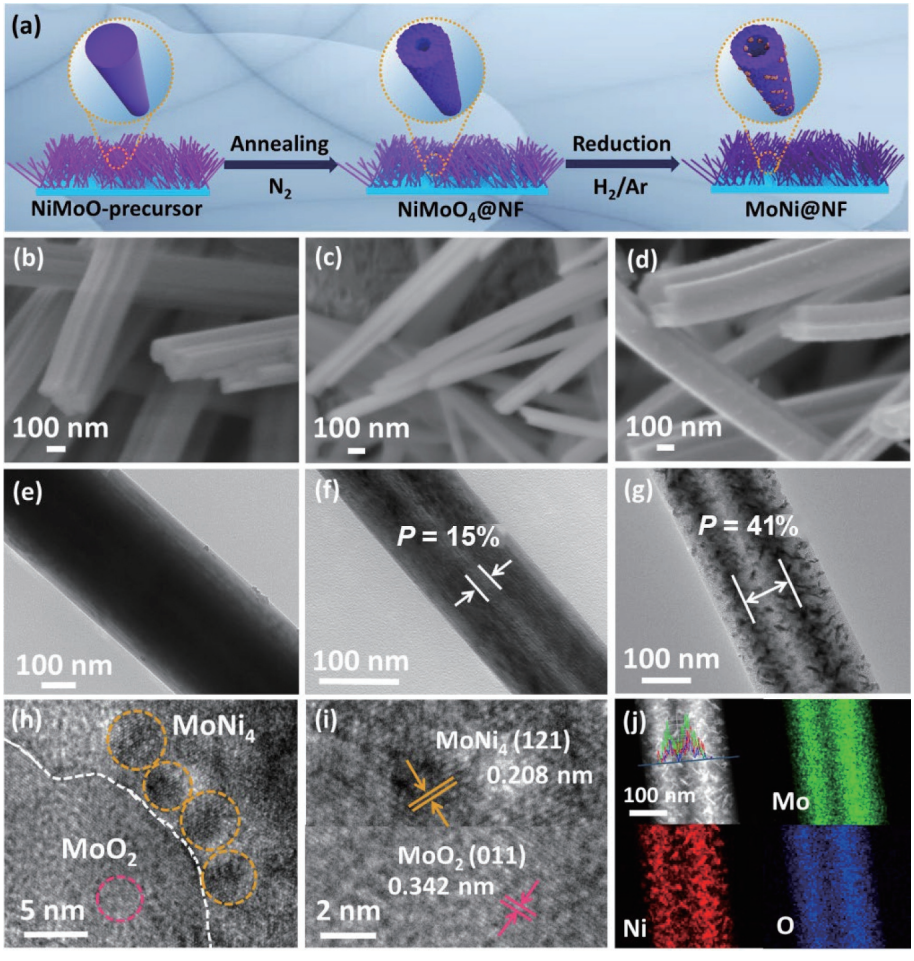

Figure 1 (a) Schematic illustration of the formation process of MoNi@NF. SEM images of (b) NiMoO-precursor, (c) $NiMoO_4$@NF, and (d) MoNi@NF. TEM images of (e) NiMoO-precursor, (f) $NiMoO_4$@NF, and (g) MoNi@NF. (h) and (i) HRTEM images of MoNi@NF. (j) TEM image with EDS line scans and corresponding elemental mappings of MoNi@NF.

diameters ranging from 200 to 500 nm, as demonstrated by SEM (Fig. 1(b)) and TEM images (Fig. 1(e)). The XRD pattern of the NiMoO-precursor reveals the formation of crystalline $NiMoO_4$ phase (PDF No. 00-009-0175) (Fig. S2 in the ESM). Second, the NiMoO-precursor is annealed under an N_2 flow at 450 °C for 3 h, and the obtained $NiMoO_4$@NF is also composed of well-dispersed nanorods with the diameters ranging from 150 to 450 nm, in which the $NiMoO_4$ phase with high crystallinity is demonstrated from the XRD pattern (Fig. 1(c) and Fig. S3 in the ESM). It is interesting that the nanorod, producing hollow cavity with the hollow diameter accounting for 15% of the total diameter, is obtained after thermal annealing treatment in N_2 atmosphere due to the kirkendall effect (Fig. 1(f)). Finally, the as-synthesized hollow $NiMoO_4$@NF nanorods are reduced in a H_2/Ar atmosphere, and the obtained MoNi@NF also inherits the nanorods-like morphology with the diameters ranging from 150 to 450 nm, but with more rough surface compared to the NiMoO-precursor and $NiMoO_4$@NF (Fig. 1(d) and Fig. S4 in the ESM). TEM image of MoNi@NF shows that the proportion of the hollow diameter to the total diameter has increased from 15% to 41%, and numerous well-distributed nanoparticles with sizes in the range of 5–20 nm are uniformly dispersed on the surface of nanorods after reduction in H_2/Ar (Fig. 1(g)). The product of the $NiMoO_4$@NF calcined at H_2/Ar was further surveyed with high-resolution TEM (HRTEM) image to reveal the components of MoNi@NF. Clearly, the HRTEM images of the MoNi@NF show lattice fringes with interplanar distances of 0.342 and 0.208 nm, which correspond to the (011) facet of MoO_2 and the (121) facet of $MoNi_4$, respectively (Figs. 1(h) and 1(i)). It is worth to note that MoO_2 is generated and the inner Ni atoms diffuse outward to form $MoNi_4$ nanoparticles directly aligned on the MoO_2 nanorods. To explore the formation mechanism of the MoNi@NF nanorods with the enlarged hollow degree, structure and composition of unary Mo@NF and Ni@NF, MoNi + H_2/Ar@NF prepared by thermal reduction only in the H_2/Ar atmosphere were also investigated (Figs. S5–S11 in the ESM). In comparison with the MoNi@NF nanorods, unary Mo@NF and Ni@NF exhibit nanosheets-like morphology, and they are composed of MoO_2 and Ni, respectively (Figs. S5–S8 in the ESM). MoNi + H_2/Ar@NF, which are obtained by only one-step of thermal reduction of NiMoO-precursor, are also composed of MoO_2 and $MoNi_4$ with well-dispersed hollow nanorod-like morphology, and the proportion of the hollow diameter to the total diameter is only 28%, which is much lower than the 41% for MoNi@NF nanorods (Figs. S9–S11 in the ESM). In addition, the typical TEM and the corresponding mapping for the Mo, Ni, and O elements demonstrate the successful synthesis of hollow MoNi@NF nanorods and uniform distribution of these elements on NF (Fig. 1(j)). The above results demonstrate that the two-step of annealing followed by thermal reduction is responsible for the formation of enlarged hollow diameter for MoNi@NF nanorods and the formation of ultrafine $MoNi_4$ supported on MoO_2 hollow nanorods is inseparable with the coexistence of Mo and Ni species via the hydrothermal-annealing-reduction process.

In order to further reveal the compositions and valence states of MoNi@NF nanorods, XRD pattern and XPS analysis of MoNi@NF were also presented. As shown in Fig. 2(a), three diffraction peaks at 44.5°, 51.8°, and 76.4° in MoNi@NF can be attributed to the (111), (200), and (220) crystal facets of metallic Ni (PDF No. 00-004-0850), which mainly originate from the NF as substrates. Besides, three characteristic peaks at 43.5°, 50.4°, and 74.7°, corresponding to (121), (310), and (312) planes of the $MoNi_4$ alloy phase (PDF No. 03-065-5480), indicate the successful synthesis of highly active $MoNi_4$ alloys. Another three well-resolved peaks at 26.0°, 36.9° and, 53.4° are attributed to the (011), ($\bar{2}$11), and ($\bar{3}$11) crystal facets from the MoO_2 phase (PDF No. 03-065-5787). These results indicate the successful synthesis of $MoNi_4$ and MoO_2 supported on conductive NF, which is consistent with the HRTEM analysis. In order to gain insight into the chemical states and probe the internal bonding configuration of MoNi@NF, XPS was conducted to identify the chemical valence states on the surface of the catalysts. As displayed in Fig. S12 in the ESM, the MoNi@NF sample is consisted of Mo, Ni, C, and O elements. As shown in Fig. 2(b), the high-resolution spectrum of Mo 3d region can be deconvoluted into three separated doublets. Two peaks at 232.1 and 235.1 eV can be attributed to the Mo^{6+} of MoO_3 species, which is formed due to the surface oxidation [39]. The Mo 3d peaks at 228.7 and 231.5 eV for MoNi@NF represent the typical doublet of the Mo^0 derived from $MoNi_4$, which have shifted negatively compared with that of Mo@NF [40]. The doublet peaks at 229.8 and 233.1 eV can be indexed to the Mo^{4+} species [24], indicating the presence of MoO_2, in which the peaks have also shifted negatively compared with the value of Mo@NF, demonstrating the Mo bears some negative charge after the addition of Ni atoms (Fig. 2(b)) [41]. Analogously, the shift of peaks can also be reflected from the Ni 2p spectrum. As shown in Fig. 2(c), two obvious peaks of Ni spectrum for MoNi@NF at 855.9 and 873.7 eV are attributed to Ni^{2+} $2p_{3/2}$ and Ni^{2+} $2p_{1/2}$, respectively, and two satellite peaks are located at 861.5 and 879.8 eV, respectively [42]. The typical peak at 852.3 eV originates from Ni^0 [43], and the binding energy of Ni species in MoNi@NF is positively shifted compared with Ni@NF. The above XPS results reveal the synergistic electronic effect of Mo and Ni. For O 1s spectrum of MoNi@NF, the three diffraction peaks at 532.5, 531.1, and 530.1 eV are ascribed to absorbed water, Ni–O, and Mo–O, respectively, further demonstrating the formation of MoO_2 [39]. To further interpret the electronic modulation effect for $MoNi_4$/MoO_2 heterostructure, the density of states (DOS) for $MoNi_4$/MoO_2 heterostructure and MoO_2 were further calculated as presented in Figs. 2(e) and 2(f). After the formation of the $MoNi_4$/MoO_2 heterostructure, the DOS of MoNi@NF at the Fermi level is significantly increased compared with that of MoO_2, indicating that more charge carriers participate in the electrocatalytic reaction, which can significantly improve the catalytic performance [44]. In addition, the increased DOS at the Fermi level in the $MoNi_4$/MoO_2 heterostructure also implies a higher electrical conductivity with enhanced charge-transfer kinetic.

3.2 Investigation of electrocatalytic OER/HzOR and HER activities

To explore the electrocatalytic activity of the MoNi@NF, the HER and OER activities of as-prepared MoNi@NF were firstly evaluated by directly using these three-dimensional (3D) networked materials as working electrodes in 1.0 M KOH electrolyte on a standard three-electrode apparatus. For comparison, Mo@NF, Ni@NF, NF, and commercial Pt/C or RuO_2 catalysts with the same loading amount with MoNi@NF catalyst were also tested under the same conditions. As displayed in Figs. 3(a) and 3(b) and Fig. S13(a) in the ESM, the LSV curves demonstrate that MoNi@NF displays small overpotentials of only 56 and 219 mV to drive 100 $mA{\cdot}cm^{-2}$ and a large current density of 1,000 $mA{\cdot}cm^{-2}$ for HER, which are much lower than those of Mo@NF, Ni@NF, and even Pt/C catalyst, and also lower than those of $NiMoO_4$@NF and MoNi + H_2/Ar@NF control samples. The OER activity is also significant to pursuing bifunctional catalyst so as to simplify the processing installation. Hence, the catalytic activity of the MoNi@NF electrode to OER was also evaluated identically to HER. The LSV curves indicate that the MoNi@NF shows much higher OER activity than other control

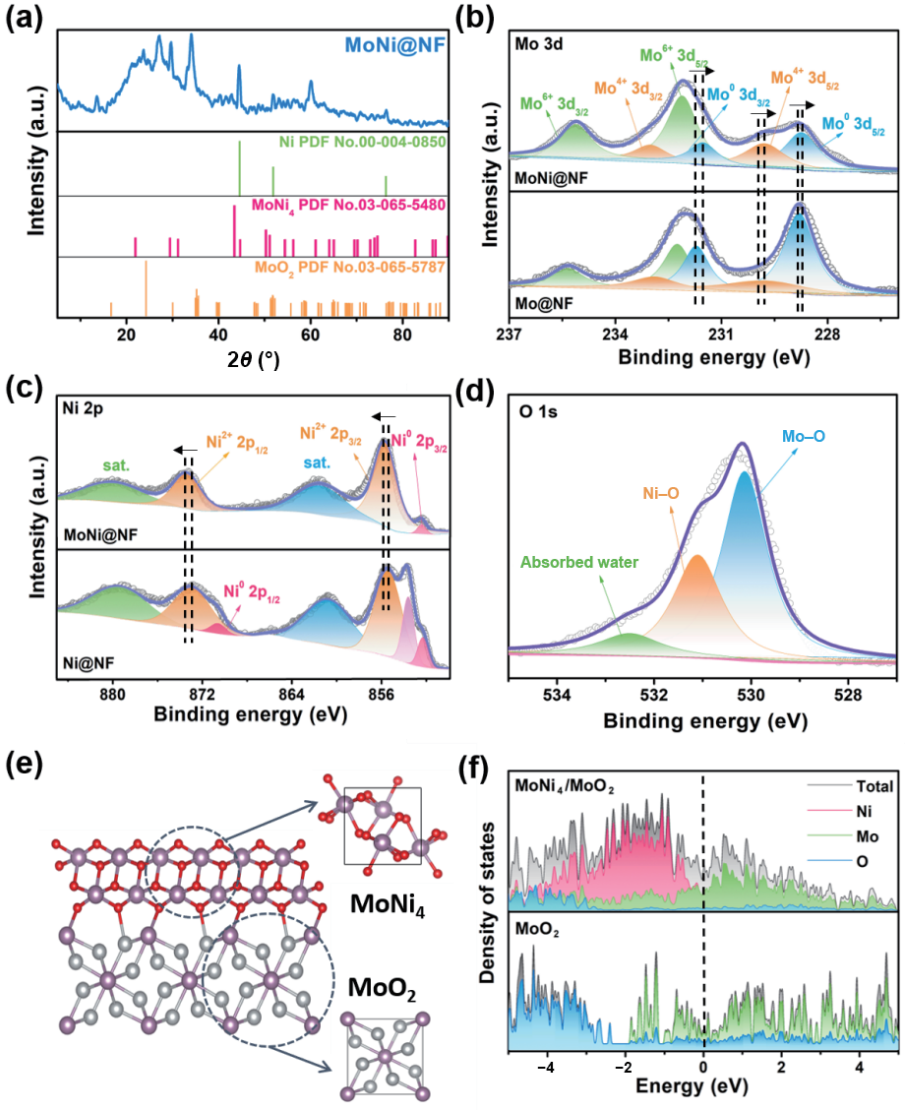

Figure 2 (a) XRD patterns of MoNi@NF. (b) Mo 3d spectra of MoNi@NF and Mo@NF. (c) Ni 2p spectra of MoNi@NF and Ni@NF. (d) O 1s spectra of MoNi@NF. (e) Optimized structure models and (f) the density of states of $MoNi_4/MoO_2$ and MoO_2.

samples and even the commercial RuO_2 catalyst in alkali media. To attain 100 mA·cm^{-2} and a large current density of 1,000 mA·cm^{-2}, MoNi@NF requires an overpotential of only 161 and 501 mV, which is much lower than that for Mo@NF, Ni@NF, and even RuO_2 catalyst, and also lower than those of $NiMoO_4$@NF and MoNi + H_2/Ar@NF, declaring the significance of MoNi alloys and the combination of annealing with high-temperature reduction process (Figs. 3(a) and 3(b) and Fig. S14(a) in the ESM). It is worth to note that the superior HER/OER activity of MoNi@NF nanorods is also well ahead of those of transitional metal-based bifunctional electrocatalysts in alkaline media reported in recent years, which are listed in Fig. 3(c) and Table S1 in the ESM. Tafel plots [η vs. log(j)] derived from LSV curves for these catalysts were used to interpret the HER kinetics (Figs. S13(b) and S15(a) in the ESM). The Tafel slope of Pt/C on NF is calculated to be about 100.9 mV·dec^{-1}, while the Tafel slope for MoNi@NF catalyst is 94.5 mV·dec^{-1}, which is smaller than those of Pt/C, Mo@NF (153.9 mV·dec^{-1}), Ni@NF (104.8 mV·dec^{-1}), $NiMoO_4$@NF (104.8 mV·dec^{-1}), and MoNi + H_2/Ar@NF (127.7 mV·dec^{-1}) control samples, indicating accelerated HER kinetics for the MoNi@NF electrode. Moreover, the Tafel slope of MoNi@NF is in the range of 40–120 mV·dec^{-1}, implying that the surface of MoNi@NF has proceeded via a Volmer-Heyrovsky mechanism [45]. In consistent with the HER results, the Tafel plots of MoNi@NF is as low as 74.1 mV·dec^{-1} during the OER process, suggesting more favorable catalytic kinetics than those of RuO_2, Mo@NF, Ni@NF, $NiMoO_4$@NF, and MoNi + H_2/Ar@NF (Figs. S14(b) and S16(a) in the ESM). In order to conclude the interfacial charge transfer kinetics, the EIS measurement was regulated to acquire the Nyquist plots for HER process (Figs. S13(c) and S15(b) in the ESM), where the MoNi@NF electrode shows a minimum charge transfer resistance of 1.2 Ω in comparison with Mo@NF, Ni@NF, $NiMoO_4$@NF, and MoNi + H_2/Ar@NF, suggesting that MoNi@NF has the most significant interfacial electron transfer kinetics during HER process. OER kinetics was also analyzed by EIS measurement. MoNi@NF electrode exhibits a smaller semicircle in the low-frequency range and a lower R_{ct} value than those of control samples, indicating the more rapid charge transfer within the MoNi@NF catalyst (Figs. S14(c) and S16(b) in the ESM). Moreover, the HER and OER performances of as-prepared samples were reflected from the electrochemical active surface area (ECSA), respectively. Through the cyclic voltammetry (CV) curves in non-Faradic region, the C_{dl} value of MoNi@NF is determined to be 9.03 and 11.51 mF·cm^{-2} for HER and OER, respectively, which is larger than those of control samples (Fig. S17 in the ESM). Such a high electrochemical capacitance of MoNi@NF strongly suggests that the hollow MoNi@NF nanorods have the

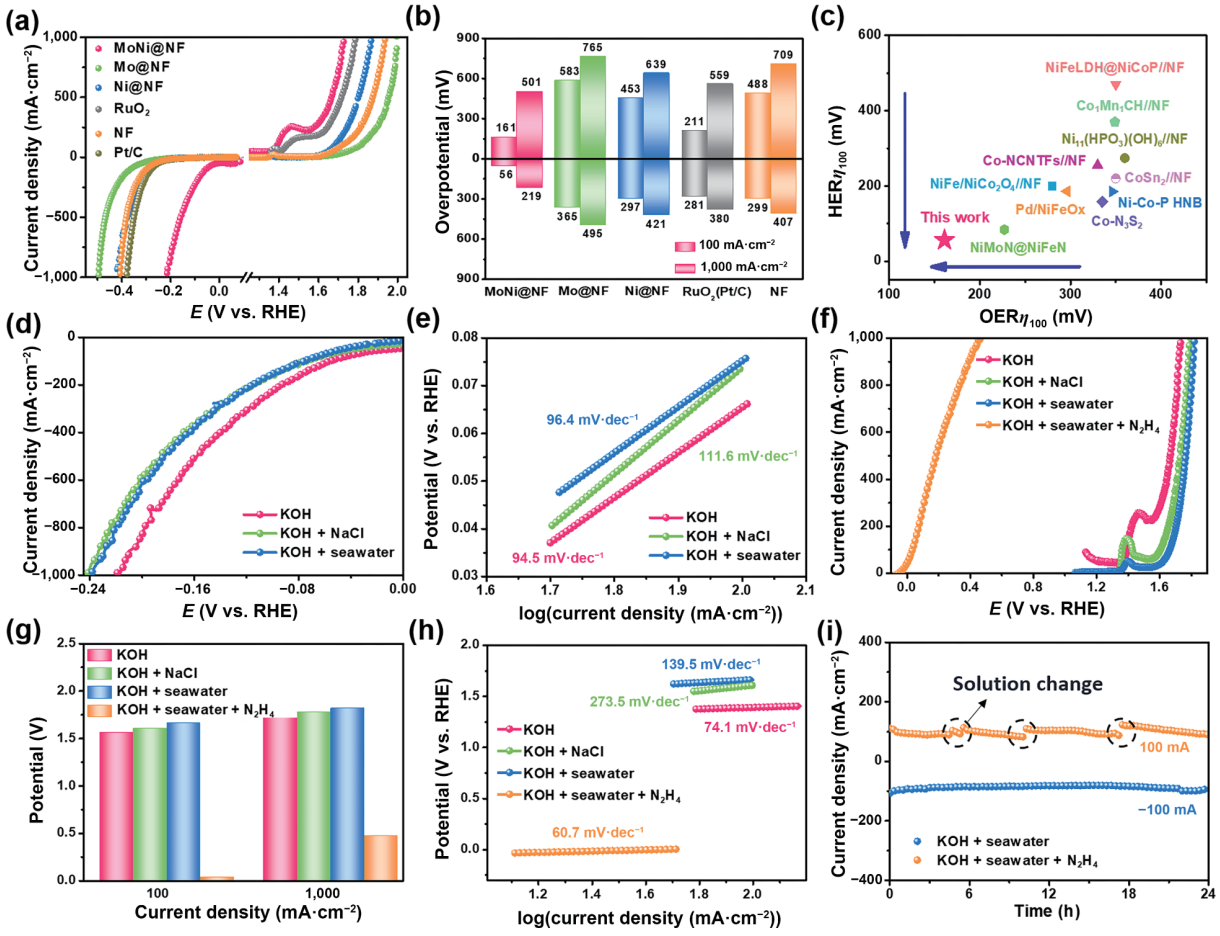

Figure 3 HER and OER performance of the as-prepared catalysts for (a) polarization curves, (b) overpotential at 100 and 1,000 mA·cm^{-2}, and (c) comparison of the overpotentials for OER (at 100 mA·cm^{-2}) and HER (at −100 mA·cm^{-2}) of the prepared MoNi@NF and other reported bifunctional electrocatalysts in 1.0 M KOH. (d) Polarization curves and (e) corresponding Tafel plots for HER in different solutions. (f) Polarization curves, (g) corresponding Tafel plots, and (h) potential at 100 and 1,000 mA·cm^{-2} in different solutions. (i) Chronoamperometry *i*–*t* curve for 24 h for HER and HzOR.

largest ECSA. Furthermore, the ECSA-normalized polarization curves (Fig. S18 and Table S4 in the ESM) show superior HER and OER performance of MoNi@NF to control samples, indicating its intrinsically improved activity. Meanwhile, the turnover frequency (TOF) reveals the intrinsic catalytic activity of each active site of the catalyst. Tables S2 and S3 in the ESM summarize the number of active sites and TOF values for HER and OER at the overpotential of 100 mV according to the CVs in Fig. S19 in the ESM. Figure S20 in the ESM shows the polarization curves that are normalized for the active sites, which are expressed in terms of TOF. It illustrates that the MoNi@NF sample can generate the most active sites for HER and OER. Correspondingly, the calculated TOF values of MoNi@NF, Mo@NF, Ni@NF, and NF are 0.40, 0.011, 0.021, and 0.025 s^{-1} for HER and 0.081, 0.0027, 0.0047, and 0.0074 s^{-1} for OER at 100 mV. It indicates that MoNi@NF not only possesses abundant electrocatalytic active sites, but also enhances the intrinsic catalytic activity.

After exploring the electrocatalytic HER and OER performance of MoNi@NF in 1.0 M KOH pure water, considering the practical application, we investigated the electrocatalytic activity of MoNi@NF in alkaline simulated seawater (1.0 M KOH + 0.5 M NaCl) and alkaline natural seawater (1.0 M KOH + seawater) from the Shilaoren Beach, Shandong, China. Besides, the effects of different solutions on the electrocatalytic performance of MoNi@NF under a standard three-electrode system were compared. As shown in Figs. 3(d) and 3(e) and Fig. S21 in the ESM, the hollow MoNi@NF nanorods show brilliant activity in both alkaline simulated seawater and natural seawater. To deliver a large current density of 1,000 mA·cm^{-2} in 1.0 M KOH + 0.5 M NaCl and 1.0 M KOH + seawater, the required potentials are only 241 and 238 mV, respectively, which are only slightly larger than that in 1.0 M KOH pure water. The Tafel slope of MoNi@NF in 1.0 M KOH + 0.5 M NaCl and 1.0 M KOH + seawater is as low as 111.6 and 96.4 mV·dec^{-1}, respectively. Then we compared the OER performance of MoNi@NF in both the alkaline simulated and natural seawater. As shown in Fig. 3(f), MoNi@NF requires a low potential of only 1.39 and 1.73 V to drive a large current density of 100 and 1,000 mA·cm^{-2} in 1.0 M KOH, respectively, and the LSV curves of the alkaline simulated seawater and natural seawater almost coincide with those of the 1.0 M KOH freshwater electrolyte, suggesting the presence of some insoluble precipitates, such as $Ca(OH)_2$ and $Mg(OH)_2$, have little damage on surface active sites in the seawater. In addition, considering commercial applications, the HER process usually requires a larger current density, even more than 1 A·cm^{-2}, so the OER potential increases with the increase of the cathode current, while the overpotential range of OER is only 480 mV without any interference from chlorine evolution. OER and chlorine precipitation may compete with each other under a large overpotential. Therefore, we coupled HzOR (0.5 M N_2H_4) at the anode to reduce the overpotential for anodic oxidation due to the low equilibrium potential of as low as −0.33 V vs. RHE. Impressively, by comparing the LSV curves of MoNi@NF in 1.0 M KOH + seawater + N_2H_4 with other alkaline electrolytes, we can clearly observe the significantly improved catalytic activity for HzOR, revealing the possibility of MoNi@NF for energy-saving hydrogen production via hydrazine oxidation assisted strategy [45]. For HzOR, MoNi@NF only needs a working potential of 360 and 470 mV to drive a current density of 100 and

1,000 mA·cm^{-2}, which is much lower than that of N_2H_4-free electrolyte (Figs. 3(f) and 3(g)). The corresponding Tafel plots indicate that the Tafel slope of MoNi@NF is greatly reduced after adding N_2H_4, indicating the fast reaction kinetics for HzOR process (Fig. 3(h)). We also investigated the polarization curves of MoNi@NF normalized by ECSA and TOF (Figs. S22 and S23 in the ESM), which indicate that MoNi@NF also displays excellent activity for HzOR with large ECSA and abundant active sites. Stability is an essential metric to evaluate the industrial application of an electrocatalyst. Therefore, we also performed an *i*–*t* test on MoNi@NF for the HER and HzOR processes at an initial current density of ~ 100 mA·cm^{-2}. As shown in Fig. 3(i), the MoNi@NF displays excellent long-term HER durability by the chronoamperometric *i*–*t* test for 24 h, in which negligible attenuation can be observed, indicating its high stability. For HzOR process, the electrolyte is changed to eliminate the effect of decreased hydrazine concentration on reaction, where negligible decay of current density can be observed, proving its excellent durability [46].

3.3 Evaluation of MoNi@NF as bifunctional catalyst for OHzS in seawater

Encouraged by the excellent electrocatalytic performance for HER and HzOR in alkaline electrolyte, a two-electrode containing self-assembled MoNi@NF as both the cathode and anode for OHzS was measured in 1.0 M KOH + seawater + 0.5 M N_2H_4 electrolyte, and commercial Pt/C||RuO_2 was also presented as comparison. Surprisingly, the required voltage of 0.54 V is needed for MoNi@NF to drive 1,000 mA·cm^{-2}, much less than that of noble metal Pt/C||RuO_2 pairs of 0.82 V (Fig. 4(a)), and the Tafel slope of MoNi@NF is measured to be 208.7 mV·dec^{-1}, also less than that of Pt/C||RuO_2 pairs (Fig. 4(b)). Specifically, the self-assembled MoNi@NF sample in the two-electrode system shows better OHzS performance than those of recently reported catalysts (Fig. 4(c)). Long-term stability is a vital parameter for evaluating the electrocatalytic performance in two-electrode systems. The chronoamperometric *i*–*t* curves with multi-current steps shown in Fig. 4(d) indicate the good stability of MoNi@NF at different current densities. In addition, as observed in Fig. 4(e), we also tested the long-term stability of the MoNi@NF couple for OHzS in seawater electrolysis by chronoamperimetric *i*–*t* test. As expected, the *i*–*t* curve delivers more than 100 mA·cm^{-2} in the beginning and remains stable for at least 100 h with no observable current density decay, exhibiting prominent durability in corrosive seawater.

Notably, in order to confirm the feasibility of employing MoNi@NF as bifunctional electrocatalyst for OHzS in alkaline seawater system to realize energy-saving hydrogen production compared with hydrazine-free systems, we firstly compared the LSV curves of MoNi@NF couple for two-electrode electrolysis in different solutions. Figure 5(a) shows the comparing LSV curves between OHzS and overall seawater splitting, where the use of HzOR to assist hydrogen production can visually improve the energy efficiency. Specifically, the MoNi@NF couple could afford

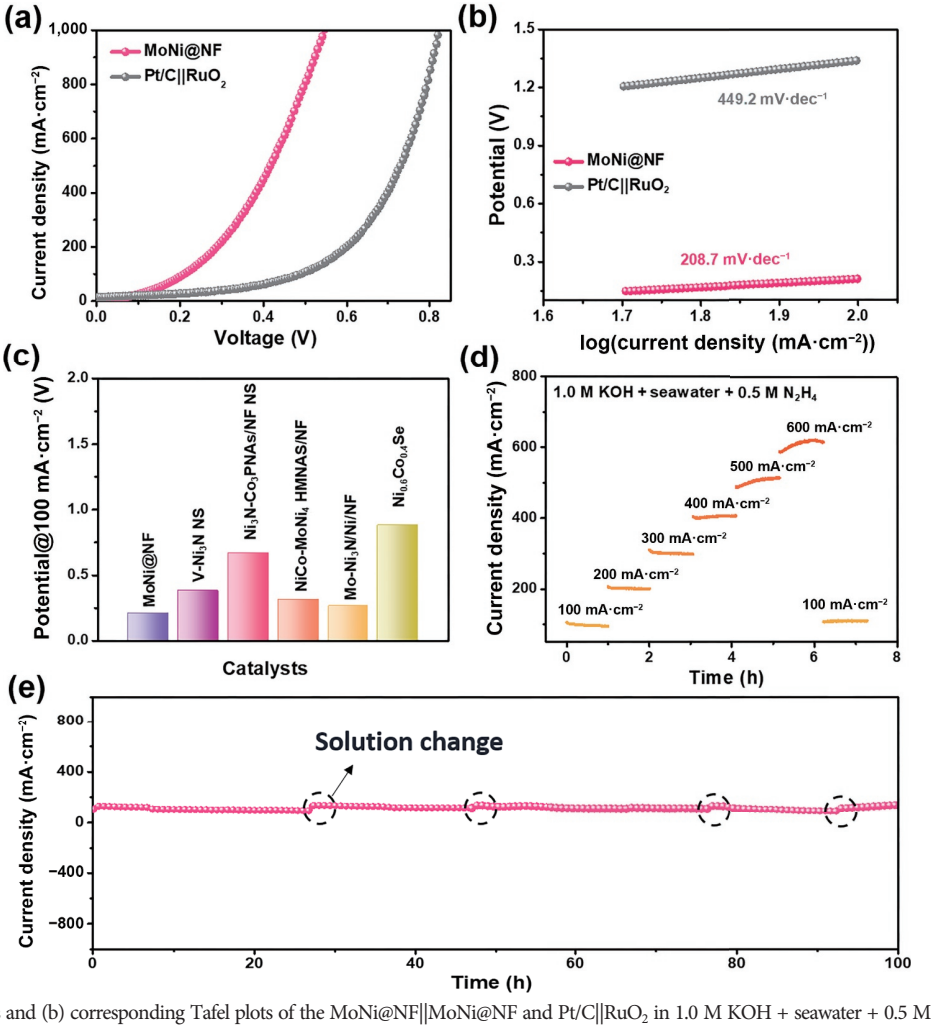

Figure 4 (a) LSV curves and (b) corresponding Tafel plots of the MoNi@NF||MoNi@NF and Pt/C||RuO_2 in 1.0 M KOH + seawater + 0.5 M N_2H_4. (c) Comparison of the overpotentials for OHzS (at 100 mA·cm^{-2}) of the prepared MoNi@NF with other reported bifunctional electrocatalysts. (d) Multi-current electrochemical process of MoNi@NF. (e) Chronoamperometry *i*–*t* curve of the MoNi@NF couple in 1.0 M KOH + seawater + N_2H_4 for 100 h.

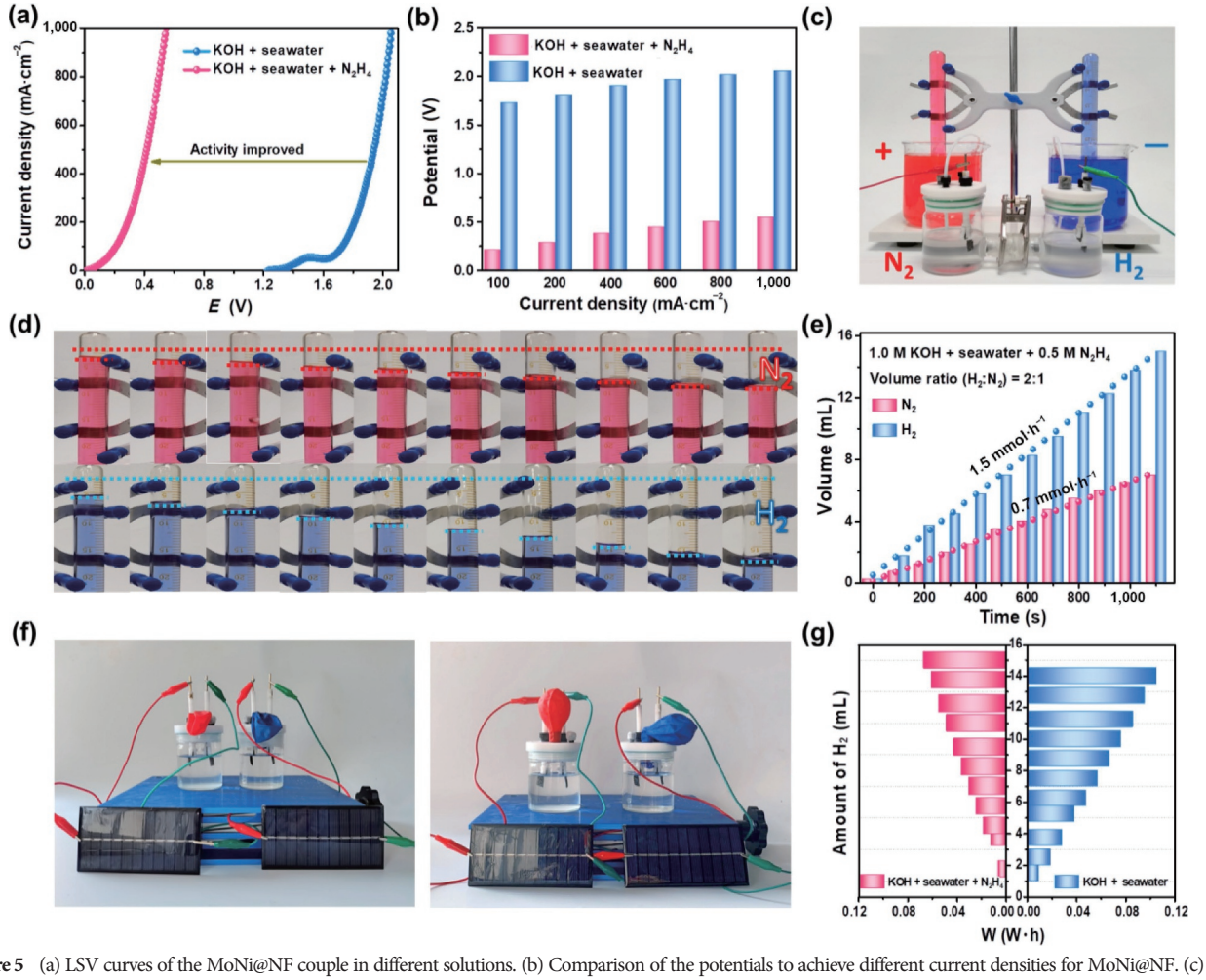

Figure 5 (a) LSV curves of the MoNi@NF couple in different solutions. (b) Comparison of the potentials to achieve different current densities for MoNi@NF. (c) The gas collection device of alkaline seawater splitting. (d) Photographs of H_2 and N_2 collected at different time points in 1.0 M KOH + seawater + 0.5 M N_2H_4. (e) The amount of H_2 and N_2 varying with time in 1.0 M KOH + seawater + 0.5 M N_2H_4. (f) Image of the electrocatalytic process powered by the solar panels. (g) The power consumption varying with amount of H_2.

a current density of 1,000 mA·cm^{-2} with an ultralow cell voltage of 0.54 V in 1 M KOH + seawater + N_2H_4 solution. In contrast, achieving the same current density in 1 M KOH + seawater requires a higher cell voltage of 2.05 V, which suggests that the electrolysis efficiency is significantly enhanced after adding N_2H_4. Compared to recently reported electrodes, the MoNi@NF still exhibits far superior OHzS activity under similar conditions (Table S5 in the ESM). Figure 5(b) intuitively reveals that the MoNi@NF couple for OHzS in seawater needs low cell voltages of 0.21, 0.28, 0.38, 0.44, 0.49, and 0.54 V to achieve current densities of 100, 200, 400, 600, 800, and 1,000 mA·cm^{-2}, respectively, yet much higher cell voltages of 1.72, 1.81, 1.90, 1.97, 2.02, and 2.05 V are needed for overall seawater splitting. Faradaic efficiency is an intuitive parameter for evaluating catalytic performance. In order to test this, a self-made water-splitting unit was constructed under 1 M KOH + seawater + 0.5 M N_2H_4 using MoNi@NF self-supported electrodes as both the cathode and the anode (Fig. 5(c)). The generated N_2 and H_2 bubbles were collected and measured by a conventional drainage method. Figure 5(d) shows the gas volume of anode and cathode at different time points and the final N_2/H_2 volume ratio of 2:1 was measured, which conforms to the theoretical value of 2:1, showing the Faraday efficiency is close to 100% in the two-electrode system and the calculated hydrogen rate is 1.5 mmol·h^{-1} at 100 mA·cm^{-2} (Fig. 5(e)). In addition, hydrogen production with cost-effectiveness and better sustainability can be realized by solar panels, which can be powered by easily harvestable and green solar energy. As depicted in Fig. 5(f), by comparing the initial with final balloon in different solutions, we can clear see that the balloon in 1 M KOH + seawater + N_2H_4 is larger than that in 1 M KOH + seawater, revealing the energy-saving hydrogen production can be realized by HzOR assistance. In order to calculate the detailed value of energy saved, the generated H_2 for MoNi@NF couple was also collected by water drainage method in 1 M KOH + seawater under the same condition with that in 1 M KOH + seawater + N_2H_4, as reflected from Fig. S24 in the ESM. As shown in Fig. 5(e) and Fig. S25 in the ESM, the amount of hydrogen produced is proportional to the reaction time, so the amount of H_2 to 1 liter is expanded to reflect the detailed value of energy saved. It can be concluded from Fig. 5(g) and Fig. S26 in the ESM that 2.94 W·h of electric energy can be saved on MoNi@NF-based electrodes to generate per liter H_2 in hydrazine oxidation assisted alkaline seawater electrolysis relative to alkaline seawater electrolysis with 37% lower energy equivalent input, demonstrating the effective energy-saving hydrogen production assisted by hydrazine oxidation.

To gain further insight into the reaction mechanism for the excellent HER and HzOR activity of the MoNi@NF catalyst, the structure, composition, and chemical state during and after HER and HzOR tests were also characterized. For HER test, it can be seen from the SEM and TEM images that the well-dispersed hollow nanorod-like morphology is intact after HER tests, indicating the stable property of MoNi@NF (Figs. S27(a) and S27(b) in the ESM). The comparing XPS spectra of MoNi@NF further confirm the existence of the Mo^{6+}, Mo^{4+}, and Mo^0 for Mo, and Ni^{2+} and Ni^0 for Ni after HER test. It is worth to note that the

atomic percentages of Mo^0 and Ni^0 increase after HER test, originating from partial reduction of Mo–O and Ni–O during HER, where the Mo^0 and Ni^0 can efficiently cleave HO–H to supply abundant H* for following reaction (Fig. 6(a)). To further confirm the partial reduction of Mo–O and Ni–O to Mo^0 and Ni^0, the *in-situ* Raman measurements were also employed to interpret the real-time evolution of the MoNi@NF catalyst during the HER process. In Fig. 6(c), when the potential is up to −0.1 V vs. RHE, at which the HER process has occured, the original peaks of Mo/Ni–O at 981 cm^{-1} has disappeared, which could be ascribed to the partial reduction of Mo/Ni–O to metallic Mo/Ni [44], which is in consistent with the XPS results. Besides, the detailed structure, composition, and chemical state for HzOR process were also characterized. As displayed in Figs. S28(a) and S28(b) in the ESM, the MoNi@NF also maintains the original hollow nanorods texture without obvious collapse or leaching after HzOR test. Likewise, the comparison of the XPS spectra of MoNi@NF before and after the stability test further confirms that the chemical states of all elements remain unchanged (Fig. 6(b)). Notably, when the potential increases from 0.7 to 1.2 V vs. RHE, no obvious peaks related to metal oxyhydroxide appear, which is not consistent with the previous reports regarding the OER process, in which broad peaks assigned to the conversion of metal compounds to metal oxyhydroxide are usually observed, thus demonstrating that OER reaction has been avoided in this potential range (Fig. 6(d)). Therefore, the MoNi@NF itself can serve as the real active sites for HzOR without the formation of metal oxyhydroxide in this process [47].

4 Conclusion

In summary, a MoNi@NF electrode with enlarged hollow diameter and rich $MoNi_4/MoO_2$ interface is designed to serve as efficient bifunctional catalyst by coupling hydrogen evolution with thermodynamically favorable hydrazine oxidation in seawater. The two-step of annealing followed by thermal reduction of precursor $NiMoO_4$ nanorods on NF is responsible for the formation of MoNi alloys supported on Mo oxides with enlarged hollow diameter, which endows the enhanced interfacial conductivity and synergistic effect, and robustness for HER coupled with HzOR in alkaline seawater system. An ultralow voltage of only 0.54 V is needed to achieve a high current density of 1,000 $mA{\cdot}cm^{-2}$ by coupling HzOR and HER in the two-electrode alkaline seawater system, which is 1.51 V less than that in a hydrazine-free system, with remarkable long-term durability for at least 100 h to keep above 100 $mA{\cdot}cm^{-2}$ and nearly 100% Faradaic efficiency. It can save 2.94 W·h on MoNi@NF-based electrodes to generate per liter H_2 relative to alkaline seawater electrolysis with 37% lower energy equivalent input. This study may show the practical impact on the energy-saving hydrogen production in unlimited seawater to realize carbon-neutral hydrogen economy.

Acknowledgements

This work is financially supported by the National Natural Science Foundation of China (Nos. 51772162 and 52072197), the Outstanding Youth Foundation of Shandong Province, China (No. ZR2019JQ14), the Youth Innovation and Technology Foundation of Shandong Higher Education Institutions, China (No. 2019KJC004), the Major Scientific and Technological Innovation Project (No. 2019JZZY020405), the Major Basic Research Program of Natural Science Foundation of Shandong Province (No. ZR2020ZD09), and the Taishan Scholar Young

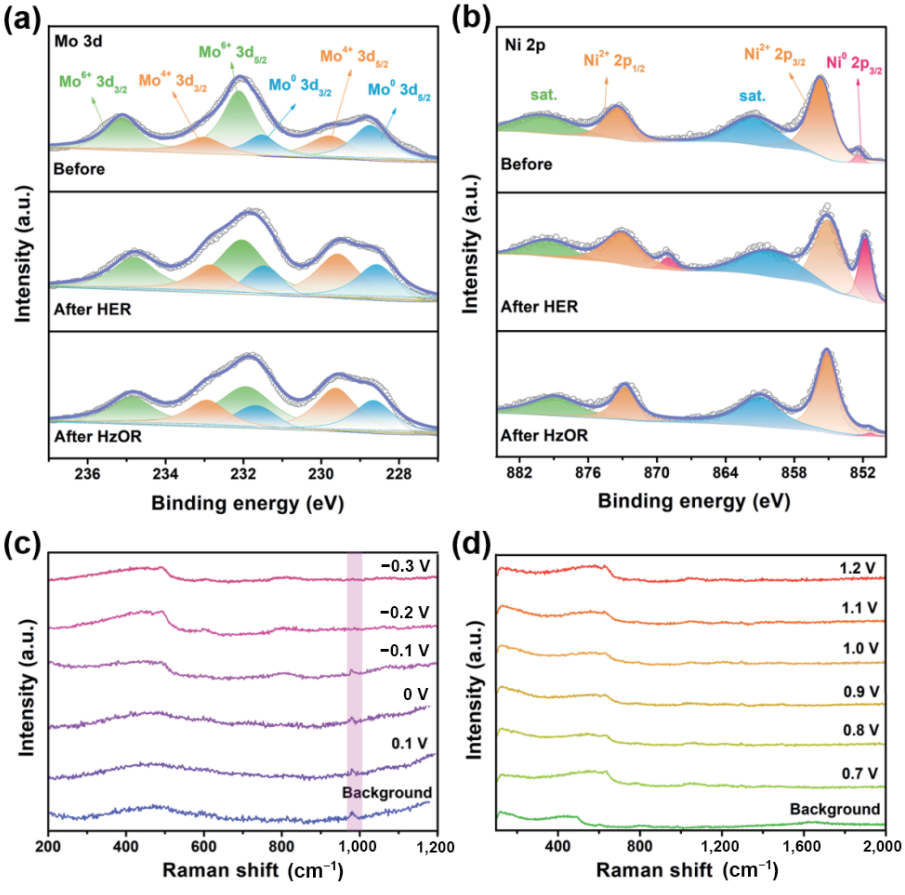

Figure 6 (a) Mo 3d spectra of MoNi@NF after HER and HzOR durability. (b) Ni 2p spectra of MoNi@NF after HER and HzOR durability. (c) *In-situ* potential-dependent Raman spectra of MoNi@NF towards HER under different potentials in 1 M KOH + seawater. (d) *In-situ* potential-dependent Raman spectra of MoNi@NF towards HzOR under different potentials in 1 M KOH + seawater + N_2H_4.

Talent Program (No. tsqn201909114).

Electronic Supplementary Material: Supplementary material (SEM images of NF, MoNi@NF, Mo@NF, Ni@NF, and MoNi + H_2/Ar@NF; TEM images of MoNi + H_2/Ar@NF; XRD patterns of NiMoO-precursor, Mo@NF, Ni@NF, and MoNi + H_2/Ar@NF; XPS survey spectra of MoNi@NF; HER, and OER performance of the MoNi@NF, $NiMoO_4$@NF, and MoNi + H_2/Ar@NF in 1.0 M KOH; photographs of H_2 and N_2 collected at different time in 1 M KOH + seawater; the amount of H_2 and N_2 varying with time in 1 M KOH + seawater; the estimated power consumption; SEM and TEM images of MoNi@NF after long-term stability test; comparison of the OER and HER activities of MoNi@NF with electrocatalysts in 1.0 M KOH solution; comparison of the HzOR activities of the MoNi@NF electrocatalysts in the alkaline electrolyte) is available in the online version of this article at https://doi.org/10.1007/s12274-022-4614-x.

References

[1] Zhao, S. L.; Wang, D. W.; Amal, R.; Dai, L. Carbon-based metal-free catalysts for key reactions involved in energy conversion and storage. *Adv. Mater.* **2019**, *31*, 1801526.

[2] Liang, H. F.; Gandi, A. N.; Xia, C.; Hedhili, M. N.; Anjum, D. H.; Schwingenschlögl, U.; Alshareef, H. N. Amorphous NiFe-OH/NiFeP electrocatalyst fabricated at low temperature for water oxidation applications. *ACS Energy Lett.* **2017**, *2*, 1035–1042.

[3] Wang, F.; Niu, S. W.; Liang, X. Q.; Wang, G. M.; Chen, M. H. Phosphorus incorporation activates the basal plane of tungsten disulfide for efficient hydrogen evolution catalysis. *Nano Res.* **2022**, *15*, 2855–2861.

[4] Zhang, X. Y.; Zhang, S.; Li, J.; Wang, E. K. One-step synthesis of well-structured NiS-$Ni_2P_2S_6$ nanosheets on nickel foam for efficient overall water splitting. *J. Mater. Chem. A* **2017**, *5*, 22131–22136.

[5] Liu, W. X.; Yu, L. H.; Yin, R. L.; Xu, X. L.; Feng, J. X.; Jiang, X.; Zheng, D.; Gao, X. L.; Gao, X. B.; Que, W. B. et al. Non-3D metal modulation of a 2D Ni-Co heterostructure array as multifunctional electrocatalyst for portable overall water splitting. *Small* **2020**, *16*, 1906775.

[6] Jiao, L.; Zhou, Y. X.; Jiang, H. L. Metal-organic framework-based CoP/reduced graphene oxide: High-performance bifunctional electrocatalyst for overall water splitting. *Chem. Sci.* **2016**, *7*, 1690–1695.

[7] Yu, W. L.; Gao, Y. X.; Chen, Z.; Zhao, Y.; Wu, Z. X.; Wang, L. Strategies on improving the electrocatalytic hydrogen evolution performances of metal phosphides. *Chin. J. Catal.* **2021**, *42*, 1876–1902.

[8] Zhao, Q. L.; Wang, Y. A.; Lai, W. H.; Xiao, F.; Lyu, Y. X.; Liao, C. Z.; Shao, M. H. Approaching a high-rate and sustainable production of hydrogen peroxide: Oxygen reduction on Co-N-C single-atom electrocatalysts in simulated seawater. *Energy Environ. Sci.* **2021**, *14*, 5444–5456.

[9] Qian, Q. Z.; Zhang, J. H.; Li, J. M.; Li, Y. P.; Jin, X.; Zhu, Y.; Liu, Y.; Li, Z. Y.; El-Harairy, A.; Xiao, C. et al. Artificial heterointerfaces achieve delicate reaction kinetics towards hydrogen evolution and hydrazine oxidation catalysis. *Angew. Chem., Int. Ed.* **2021**, *60*, 5984–5993.

[10] Ma, B.; Yang, Z. C.; Chen, Y. T.; Yuan, Z. H. Nickel cobalt phosphide with three-dimensional nanostructure as a highly efficient electrocatalyst for hydrogen evolution reaction in both acidic and alkaline electrolytes. *Nano Res.* **2019**, *12*, 375–380.

[11] Dresp, S.; Dionigi, F.; Klingenhof, M.; Strasser, P. Direct electrolytic splitting of seawater: Opportunities and challenges. *ACS Energy Lett.* **2019**, *4*, 933–942.

[12] Chen, L. F.; Hou, C. C.; Zou, L. L.; Kitta, M.; Xu, Q. Uniformly bimetal-decorated holey carbon nanorods derived from metal-organic framework for efficient hydrogen evolution. *Sci. Bull.* **2021**, *66*, 170–178.

[13] Menezes, P. W.; Panda, C.; Loos, S.; Bunschei-Bruns, F.; Walter, C.; Schwarze, M.; Deng, X. H.; Dau, H.; Driess, M. A structurally versatile nickel phosphite acting as a robust bifunctional electrocatalyst for overall water splitting. *Energy Environ. Sci.* **2018**, *11*, 1287–1298.

[14] Yu, L.; Zhu, Q.; Song, S. W.; McElhenny, B.; Wang, D. Z.; Wu, C. Z.; Qin, Z. J.; Bao, J. M.; Yu, Y.; Chen, S. et al. Non-noble metal-nitride based electrocatalysts for high-performance alkaline seawater electrolysis. *Nat. Commun.* **2019**, *10*, 5106.

[15] Sun, H. M.; Xu, X. B.; Yan, Z. H.; Chen, X.; Cheng, F. Y.; Weiss, P. S.; Chen, J. Porous multishelled Ni_2P hollow microspheres as an active electrocatalyst for hydrogen and oxygen evolution. *Chem. Mater.* **2017**, *29*, 8539–8547.

[16] Han, L. L.; Guo, L. M.; Dong, C. Q.; Zhang, C.; Gao, H.; Niu, J. Z.; Peng, Z. Q.; Zhang, Z. H. Ternary mesoporous cobalt-iron-nickel oxide efficiently catalyzing oxygen/hydrogen evolution reactions and overall water splitting. *Nano Res.* **2019**, *12*, 2281–2287.

[17] Lv, C. N.; Zhang, L.; Huang, X. H.; Zhu, Y. X.; Zhang, X.; Hu, J. S.; Lu, S. Y. Double functionalization of N-doped carbon carved hollow nanocubes with mixed metal phosphides as efficient bifunctional catalysts for electrochemical overall water splitting. *Nano Energy* **2019**, *65*, 103995.

[18] Song, Y. Y.; Cheng, J. L.; Liu, J.; Ye, Q.; Gao, X.; Lu, J. J.; Cheng, Y. L. Modulating electronic structure of cobalt phosphide porous nanofiber by ruthenium and nickel dual doping for highly-efficiency overall water splitting at high current density. *Appl. Catal. B Environ.* **2021**, *298*, 120488.

[19] Xing, J. N.; Lin, F.; Huang, L. T.; Si, Y. C.; Wang, Y. J.; Jiao, L. F. Coupled cobalt-doped molybdenum carbide@N-doped carbon nanosheets/nanotubes supported on nickel foam as a binder-free electrode for overall water splitting. *Chin. J. Catal.* **2019**, *40*, 1352–1359.

[20] Wu, L. B.; Yu, L.; Zhang, F. H.; McElhenny, B.; Luo, D.; Karim, A.; Chen, S.; Ren, Z. F. Heterogeneous bimetallic phosphide Ni_2P-Fe_2P as an efficient bifunctional catalyst for water/seawater splitting. *Adv. Funct. Mater.* **2021**, *31*, 2006484.

[21] Zhao, Y.; Gao, Y. X.; Chen, Z.; Li, Z. J.; Ma, T. Y.; Wu, Z. X.; Wang, L. Trifle Pt coupled with NiFe hydroxide synthesized via corrosion engineering to boost the cleavage of water molecule for alkaline water-splitting. *Appl. Catal. B Environ.* **2021**, *297*, 120395.

[22] Yao, M. Q.; Wang, B. J.; Sun, B. L.; Luo, L. F.; Chen, Y. J.; Wang, J. W.; Wang, N.; Komarneni, S.; Niu, X. B.; Hu, W. B. et al. Rational design of self-supported Cu@WC core–shell mesoporous nanowires for pH-universal hydrogen evolution reaction. *Appl. Catal. B Environ.* **2021**, *280*, 119451.

[23] Dong, B.; Xie, J. Y.; Tong, Z.; Chi, J. Q.; Zhou, Y. N.; Ma, X.; Lin, Z. Y.; Wang, L.; Chai, Y. M. Synergistic effect of metallic nickel and cobalt oxides with nitrogen-doped carbon nanospheres for highly efficient oxygen evolution. *Chin. J. Catal.* **2020**, *41*, 1782–1789.

[24] Li, Y. P.; Li, J. M.; Qian, Q. Z.; Jin, X.; Liu, Y.; Li, Z. Y.; Zhu, Y.; Guo, Y. M.; Zhang, G. Q. Superhydrophilic Ni-based multicomponent nanorod-confined-nanoflake array electrode achieves waste-battery-driven hydrogen evolution and hydrazine oxidation. *Small* **2021**, *17*, 2008148.

[25] Chala, S. A.; Tsai, M. C.; Olbasa, B. W.; Lakshmanan, K.; Huang, W. H.; Su, W. N.; Liao, Y. F.; Lee, J. F.; Dai, H. J.; Hwang, B. J. Tuning dynamically formed active phases and catalytic mechanisms of *in situ* electrochemically activated layered double hydroxide for oxygen evolution reaction. *ACS Nano* **2021**, *15*, 14996–15006.

[26] Sun, F.; Qin, J. S.; Wang, Z. Y.; Yu, M. Z.; Wu, X. H.; Sun, X. M.; Qiu, J. S. Energy-saving hydrogen production by chlorine-free hybrid seawater splitting coupling hydrazine degradation. *Nat. Commun.* **2021**, *12*, 4182.

[27] Dang, Y. L.; Wu, T. L.; Tan, H. Y.; Wang, J. L.; Cui, C.; Kerns, P.; Zhao, W.; Posada, L.; Wen, L. Y.; Suib, S. L. Partially reduced Ru/RuO_2 composites as efficient and pH-universal electrocatalysts for hydrogen evolution. *Energy Environ. Sci.* **2021**, *14*, 5433–5443.

[28] Tang, T.; Jiang, W. J.; Niu, S.; Liu, N.; Luo, H.; Chen, Y. Y.; Jin, S. F.; Gao, F.; Wan, L. J.; Hu, J. S. Electronic and morphological dual modulation of cobalt carbonate hydroxides by Mn doping toward highly efficient and stable bifunctional electrocatalysts for overall

water splitting. *J. Am. Chem. Soc.* **2017**, *139*, 8320–8328.
[29] Wang, Q.; Huang, X.; Zhao, Z. L.; Wang, M. Y.; Xiang, B.; Li, J.; Feng, Z. X.; Xu, H.; Gu, M. Ultrahigh-loading of Ir single atoms on NiO matrix to dramatically enhance oxygen evolution reaction. *J. Am. Chem. Soc.* **2020**, *142*, 7425–7433.
[30] Chen, Y. Y.; Zhang, Y.; Zhang, X.; Tang, T.; Luo, H.; Niu, S.; Dai, Z. H.; Wan, L. J.; Hu, J. S. Self-templated fabrication of $MoNi_4/MoO_{3-x}$ nanorod arrays with dual active components for highly efficient hydrogen evolution. *Adv. Mater.* **2017**, *29*, 1703311.
[31] Su, L. X.; Gong, D.; Yao, N.; Li, Y. B.; Li, Z.; Luo, W. Modification of the intermediate binding energies on Ni/Ni_3N heterostructure for enhanced alkaline hydrogen oxidation reaction. *Adv. Funct. Mater.* **2021**, *31*, 2106156.
[32] Song, L. T.; Zheng, T. L.; Zheng, L. R.; Lu, B.; Chen, H. Q.; He, Q. G.; Zheng, W. Z.; Hou, Y.; Lian, J. L.; Wu, Y. et al. Cobalt-doped basic iron phosphate as bifunctional electrocatalyst for long-life and high-power-density rechargeable zinc-air batteries. *Appl. Catal. B Environ.* **2022**, *300*, 120712.
[33] Singh, V. K.; Gupta, U.; Mukherjee, B.; Chattopadhyay, S.; Das, S. MoS_2 nanosheets on $MoNi_4/MoO_2$ nanorods for hydrogen evolution. *ACS Appl. Nano Mater.* **2021**, *4*, 886–896.
[34] Wu, X. F.; Li, J. W.; Li, Y.; Wen, Z. H. NiFeP-MoO_2 hybrid nanorods on nickel foam as high-activity and high-stability electrode for overall water splitting. *Chem. Eng. J.* **2021**, *409*, 128161.
[35] Kamp, C. J.; Perez Garza, H. H.; Fredriksson, H.; Kasemo, B.; Andersson, B.; Skoglundh, M. Nanofabricated catalyst particles for the investigation of catalytic carbon oxidation by oxygen spillover. *Langmuir* **2017**, *33*, 4903–4912.
[36] Ananyev, M. V.; Porotnikova, N. M.; Eremin, V. A.; Kurumchin, E. K. Interaction of O_2 with LSM-YSZ composite materials and oxygen spillover effect. *ACS Catal.* **2021**, *11*, 4247–4262.
[37] Gaigneaux, E. M.; Ruiz, P.; Delmon, B. Further on the mechanism of the synergy between MoO_3 and α-Sb_2O_4 in the selective oxidation of isobutene to methacrolein: Reconstuction of MoO_3 via spillover oxygen. *Catal. Today* **1996**, *32*, 37–46.
[38] Meng, L. S.; Li, L. P.; Wang, J. H.; Fu, S. X.; Zhang, Y. L.; Li, J.; Xue, C. L.; Wei, Y. H.; Li, G. S. Valence-engineered $MoNi_4/MoO_x$@NF as a Bi-functional electrocatalyst compelling for urea-assisted water splitting reaction. *Electrochim. Acta* **2020**, *350*, 136382.
[39] Yan, G.; Gu, Y. F.; Shaga, A.; Wang, K.; Zhan, L. J.; Liu, Z. M. Improving hydrogen evolution activity of two-dimensional nanosheets $MoNi_4/MoO_{2.5}$-NF self-supporting electrocatalyst by electrochemical-cycling activation. *J. Mater. Sci.* **2021**, *56*, 6945–6954.
[40] Zhang, J.; Wang, T.; Liu, P.; Liao, Z. Q.; Liu, S. H.; Zhuang, X. D.; Chen, M. W.; Zschech, E.; Feng, X. L. Efficient hydrogen production on $MoNi_4$ electrocatalysts with fast water dissociation kinetics. *Nat. Commun.* **2017**, *8*, 15437.
[41] Wang, M.; Yang, H.; Shi, J. N.; Chen, Y. F.; Zhou, Y.; Wang, L. G.; Di, S. J.; Zhao, X.; Zhong, J.; Cheng, T. et al. Alloying nickel with molybdenum significantly accelerates alkaline hydrogen electrocatalysis. *Angew. Chem., Int. Ed.* **2021**, *60*, 5771–5777.
[42] Yu, Z. Y.; Lang, C. C.; Gao, M. R.; Chen, Y.; Fu, Q. Q.; Duan, Y.; Yu, S. H. Ni-Mo-O nanorod-derived composite catalysts for efficient alkaline water-to-hydrogen conversion via urea electrolysis. *Energy Environ. Sci.* **2018**, *11*, 1890–1897.
[43] Wang, Z. J.; Guo, P.; Cao, S. F.; Chen, H. Y.; Zhou, S. N.; Liu, H. H.; Wang, H. W.; Zhang, J. B.; Liu, S. Y.; Wei, S. X. et al. Contemporaneous inverse manipulation of the valence configuration to preferred Co^{2+} and Ni^{3+} for enhanced overall water electrocatalysis. *Appl. Catal. B Environ.* **2021**, *284*, 119725.
[44] Cheng, Y.; Guo, H. R.; Yuan, P. F.; Li, X. P.; Zheng, L. R.; Song, R. Self-supported bifunctional electrocatalysts with Ni nanoparticles encapsulated in vertical N-doped carbon nanotube for efficient overall water splitting. *Chem. Eng. J.* **2021**, *413*, 127531.
[45] Du, W.; Shi, Y. M.; Zhou, W.; Yu, Y. F.; Zhang, B. Unveiling the *in situ* dissolution and polymerization of Mo in Ni_4Mo alloy for promoting the hydrogen evolution reaction. *Angew. Chem., Int. Ed.* **2021**, *60*, 7051–7055.
[46] Pan, U. N.; Paudel, D. R.; Kumar Das, A.; Singh, T. I.; Kim, N. H.; Lee, J. H. Ni-nanoclusters hybridized 1T-Mn-VTe_2 mesoporous nanosheets for ultra-low potential water splitting. *Appl. Catal. B Environ.* **2022**, *301*, 120780.
[47] Liu, Y.; Zhang, J. H.; Li, Y. P.; Qian, Q. Z.; Li, Z. Y.; Zhu, Y.; Zhang, G. Q. Manipulating dehydrogenation kinetics through dual-doping Co_3N electrode enables highly efficient hydrazine oxidation assisting self-powered H_2 production. *Nat. Commun.* **2020**, *11*, 1853.